

PROJECTED SOBOLEV NATURAL GRADIENT DESCENT FOR EFFICIENT NEURAL NETWORK SOLUTION OF THE GROSS–PITAEVSKII EQUATION*

CHENGLONG BAO[†], CHEN CUI[‡], KAI JIANG[§], AND SHI SHU[§]

Abstract. This paper introduces a projected Sobolev natural gradient descent (NGD) method for computing ground states of the Gross–Pitaevskii equation. By projecting a continuous Riemannian Sobolev gradient flow onto the normalized neural network tangent space, we derive a discrete NGD algorithm that preserves the normalization constraint. The numerical implementation employs variational Monte Carlo with a hybrid sampling strategy to accurately account for the normalization constant arising from nonlinear interaction terms. To enhance computational efficiency, a matrix-free Nyström-preconditioned conjugate gradient solver is adopted to approximate the NGD operator without explicit matrix assembly. Numerical experiments demonstrate that the proposed method converges significantly faster than physics-informed neural network approaches and exhibits linear scalability with respect to spatial dimensions. Moreover, the resulting neural-network solutions provide high-quality initial guesses that substantially accelerate subsequent refinement by traditional high-precision solvers.

Key words. Gross–Pitaevskii equation, Deep neural networks, Variational Monte Carlo, Riemannian optimization, Natural gradient descent, Preconditioning

MSC codes. 65N30, 65K10, 81Q05, 68T07

1. Introduction. Bose–Einstein condensation (BEC) is a macroscopic quantum phenomenon that emerges when a large ensemble of identical bosons occupies a single quantum ground state at ultracold temperatures. Since its first experimental realization in 1995 [1], BEC has evolved into a central platform for investigating macroscopic quantum coherence, superfluidity, and quantum simulation. Within the mean-field approximation, the macroscopic wavefunction, or order parameter, of a BEC is governed by the Gross–Pitaevskii equation (GPE) [39]. The GPE is a nonlinear Schrödinger equation featuring a cubic nonlinearity induced by effective short-range interactions. Computing the ground states of the GPE is a fundamental yet challenging problem in both theory and numerical analysis. From a mathematical perspective, this task entails minimizing a highly non-convex energy functional over a Riemannian manifold defined by a normalization constraint. The intrinsic nonlinearity of the interaction term leads to severe ill-conditioning of the energy landscape, thereby significantly complicating robust and efficient numerical optimization.

Existing numerical methods for computing GPE ground states can be broadly classified into two methodological paradigms. The first follows a discretize-then-solve

* Submitted to the editors DATE.

Funding: C.Bao was supported by the National Key R&D Program of China (2021YFA1001300), the National Natural Science Foundation of China (12271291). K.Jiang was supported by the the National Key R&D Program of China (2023YFA1008802), the Science and Technology Innovation Program of Hunan Province (2024RC1052). S.Shu was supported in part by the National Natural Science Foundation of China (12371373), the Science Challenge Project (TZ2024009).

[†]Yau Mathematical Sciences Center, Tsinghua University, Yanqi Lake Beijing Institute of Mathematical Sciences and Applications, Beijing, China, 100084.

[‡]Yau Mathematical Sciences Center, Tsinghua University, Beijing, China, 100084.(Corresponding author: chencui@mail.tsinghua.edu.cn)

[§]Hunan Key Laboratory for Computation and Simulation in Science and Engineering, Key Laboratory of Intelligent Computing and Information Processing of Ministry of Education, School of Mathematics and Computational Science, Xiangtan University, Xiangtan, Hunan, China, 411105.

philosophy, in which the continuous problem is reduced through spatial discretization to a nonlinear eigenvalue problem that is subsequently treated by algebraic techniques, including self-consistent field iterations [19, 9] and inverse iteration schemes [32]. The second paradigm adopts an optimize-then-discretize viewpoint, whereby the continuous energy functional is minimized directly under the manifold constraint. Prominent representatives of this class include projected Sobolev gradient methods [5, 25, 15, 29, 12], Riemannian conjugate gradient algorithms [2, 16, 47], momentum-accelerated schemes [11], and a variety of preconditioning strategies [2, 22]. A comprehensive overview of these methods can be found in [28].

Despite their maturity, the performance of these algorithms deteriorates in extreme physical regimes and in high-dimensional settings. In the presence of strong interactions or highly heterogeneous external potentials, the GPE energy landscape becomes severely ill-conditioned, which often leads to stagnation or convergence to spurious local minima [46]. Moreover, although the GPE is conventionally formulated in physical space, the investigation of its high-dimensional extensions is of both physical and numerical relevance. On the physical side, modern research directions such as multicomponent spinor condensates [53] and quantum Hall physics in synthetic dimensions [45] naturally give rise to nonlinear Schrödinger equations posed in dimensions exceeding three. From a numerical standpoint, high-dimensional formulations are often necessary for modeling quasi-periodic potentials, where auxiliary dimensions are introduced to restore periodicity [33]. In these contexts, classical grid-based discretizations are hampered by the curse of dimensionality, as their memory footprint and computational cost increase exponentially with the dimension, rendering them impractical for large-scale simulations.

In recent years, deep neural networks (DNNs) have achieved notable success in scientific computing due to their strong approximation capabilities for high-dimensional problems [49, 18, 55, 54]. Motivated by these advances, several neural approaches tailored to the GPE have been proposed that exploit its structural and geometric properties [4, 37]. For example, the norm-DNN method [4] enhances physics-informed neural networks (PINNs) [49] by incorporating an explicit normalization layer. However, the direct application of such PINN-based methodologies to the GPE encounters two significant challenges. First, these approaches typically rely on fixed or uniformly sampled collocation points to evaluate the residual-based loss function. In high-dimensional domains, particularly when solutions exhibit strong spatial localization, such as propagating wavefronts or concentrated probability densities, random sampling strategies frequently fail to capture physically relevant regions. Consequently, the resulting gradients tend to vanish at the majority of sampled points, leading to stagnation in parameter updates. Second, training is generally performed using first-order optimization algorithms, such as Adam [36], which often exhibit slow convergence and limited robustness when confronting the severe ill-conditioning characteristic of high-dimensional energy landscapes.

To circumvent the sampling limitations inherent in collocation-based schemes, neural network representations of wavefunctions, commonly termed neural quantum states (NQS), have emerged as a compelling alternative. In the context of linear quantum many-body physics, NQS combined with neural variational Monte Carlo (VMC) methods [10] have achieved state-of-the-art performance, with notable successes including FermiNet [48] and PauliNet [31]. In contrast to PINNs, VMC naturally handles high-dimensional integration via importance sampling from the wavefunction-induced distribution and structurally enforces normalization. However, extending this paradigm to the GPE presents distinct difficulties. Unlike the linear Schrödinger

equation, the GPE includes a nonlinear interaction term that complicates the construction of low-variance gradient estimators.

From an optimization perspective, recent years have witnessed the development of several high-performance optimization methods, including evolutional DNNs [21, 35, 34, 57], neural Galerkin methods [8, 6, 38], and natural gradient descent (NGD) methods [41, 56, 7, 44, 13, 50, 26, 17]. These approaches are fundamentally grounded in the Dirac–Frenkel variational principle (DFVP) [20, 24], which provides a systematic mechanism for projecting continuous-time dynamics onto finite-dimensional parameter manifolds. Although existing studies have explored various aspects of these methods—including metric selection, temporal discretization, and efficient approximations of the associated metric matrices—their direct application to the GPE remains highly nontrivial. The strong nonlinearities and stringent normalization constraints intrinsic to the GPE demand a more specialized and carefully designed integration of variational optimization techniques, an issue that remains largely unresolved in the current literature.

In this work, we propose a projected Sobolev NGD method within a neural VMC framework for computing ground states of high-dimensional GPE. Rather than viewing neural network training as a purely Euclidean optimization problem in parameter space, we adopt an *optimize-then-discretize* strategy that is rooted in the intrinsic geometry of the normalized function manifold. Starting from a projected Sobolev gradient flow formulation, we derive natural gradient dynamics in parameter space via the DFVP [20, 24]. This construction rigorously preserves the geometric constraints and establishes a connection between continuous functional optimization and discrete parameter updates, as illustrated in [Figure 1](#). To address the challenges arising from strong nonlinearity and high dimensionality, we develop an efficient numerical implementation that resolves several key computational bottlenecks. Specifically, a hybrid sampling strategy combining Markov chain Monte Carlo (MCMC) with adaptive defensive importance sampling is employed to obtain unbiased estimates of both the energy gradient and the associated Gram matrix. Meanwhile, a matrix-free Nyström-preconditioned conjugate gradient solver is used to avoid the explicit construction and inversion of Gram matrices, thereby reducing the per-iteration computational complexity and significantly improving scalability. The numerical results demonstrate three main advantages of the proposed framework. First, compared with existing approaches such as norm-DNN, the method achieves faster convergence, often by an order of magnitude (see [Table 4](#)). Second, the optimized neural-network solution provides a high-quality initial guess for traditional high-precision numerical solvers, leading to a pronounced reduction in iteration counts and overall time to convergence (see [Figure 5](#)). Finally, the framework exhibits excellent scalability in high dimensions, with both computational time and memory consumption growing approximately linearly with the spatial dimension, thereby effectively mitigating the curse of dimensionality (see [Figure 6](#)).

The remainder of this paper is organized as follows. [Section 2](#) states the variational framework for the GPE and formulates the continuous projected Sobolev gradient flow. [Section 3](#) details the neural network discretization and derives the NGD method. [Section 4](#) discusses the practical numerical implementation within a VMC framework, covering gradient estimation, adaptive importance sampling for the partition function, and randomized preconditioning strategies for the associated Gram matrix. [Section 5](#) presents numerical experiments to evaluate the performance of the proposed method. Finally, [Section 6](#) concludes the paper and discusses future research directions.

2. Variational formulation and Sobolev gradient flow. This section reviews the variational framework of the GPE and presents the continuous projected Sobolev gradient flow that serves as the analytical foundation for the subsequent neural discretization.

2.1. Gross–Pitaevskii energy functional and ground state problem. The dimensionless GPE posed on a bounded domain $\mathcal{D} \subset \mathbb{R}^d$ models the macroscopic behavior of a BEC in the mean-field approximation at zero temperature. The system is governed by the Gross–Pitaevskii energy functional

$$(2.1) \quad E(\psi) = \int_{\mathcal{D}} \left(\frac{1}{2} |\nabla \psi(\mathbf{r})|^2 + V(\mathbf{r}) |\psi(\mathbf{r})|^2 + \frac{\beta}{2} |\psi(\mathbf{r})|^4 \right) d\mathbf{r},$$

where $\psi : \mathcal{D} \rightarrow \mathbb{R}$ is the condensate wavefunction subject to the mass constraint $\|\psi\|_{L^2(\mathcal{D})}^2 = 1$. The parameter $\beta \in \mathbb{R}$ represents the dimensionless interaction strength, where $\beta > 0$ corresponds to the repulsive interactions investigated in this work and $\beta < 0$ models attractive interactions. The external potential $V(\mathbf{r})$ is assumed to be real-valued and confining, meaning it is bounded from below and satisfies $\lim_{|\mathbf{r}| \rightarrow \infty} V(\mathbf{r}) = +\infty$. We impose homogeneous Dirichlet boundary conditions $\psi = 0$ on $\partial\mathcal{D}$ and consider the state space $H_0^1(\mathcal{D})$.

The ground state is defined as the global energy minimizer on the unit L^2 sphere,

$$(2.2) \quad \psi_{\text{GS}} = \arg \min_{\psi \in \mathbb{S}} E(\psi), \quad \mathbb{S} := \left\{ \psi \in H_0^1(\mathcal{D}) : \|\psi\|_{L^2(\mathcal{D})}^2 = 1 \right\}.$$

Under the stated hypotheses on V and for $\beta \geq 0$, the functional E is coercive on $H_0^1(\mathcal{D})$ and weakly lower semicontinuous on \mathbb{S} , which ensures the existence of minimizers. Critical points of E on \mathbb{S} correspond to stationary states and satisfy a constrained variational principle. By introducing a Lagrange multiplier $\mu \in \mathbb{R}$, these states satisfy $\delta(E(\psi) - \mu(\|\psi\|_{L^2}^2 - 1)) = 0$. The first variation in a direction $v \in H_0^1(\mathcal{D})$ is given by

$$(2.3) \quad \langle E'(\psi), v \rangle = \int_{\mathcal{D}} (\nabla \psi \cdot \nabla v + V \psi v + \beta |\psi|^2 \psi v) d\mathbf{r},$$

leading to the nonlinear eigenvalue problem

$$(2.4) \quad H[\psi]\psi := \left(-\frac{1}{2} \Delta + V(\mathbf{r}) + \beta |\psi|^2 \right) \psi = \mu \psi.$$

For a ground state ψ_{GS} , the associated chemical potential satisfies $\mu = E(\psi_{\text{GS}}) + \frac{\beta}{2} \|\psi_{\text{GS}}\|_{L^4(\mathcal{D})}^4$. The eigenfunction ψ_{GS} is unique up to a global sign and can be chosen as strictly positive in \mathcal{D} .

2.2. Projected Sobolev gradient flow and metric selection. To compute ground states while maintaining the mass constraint, we formulate a Riemannian projected Sobolev gradient flow [28] that integrates metric preconditioning with an exact projection onto the tangent space of \mathbb{S} . The tangent space at ψ is defined as

$$T_{\psi} \mathbb{S} = \left\{ v \in H_0^1(\mathcal{D}) : (\psi, v)_{L^2} = \int_{\mathcal{D}} \psi v d\mathbf{r} = 0 \right\}.$$

Since the unconstrained first variation $E'(\psi)$ lives in the dual space $H^{-1}(\mathcal{D})$, we select a Hilbert space X compactly embedded in $L^2(\mathcal{D})$ and identify the Riesz representer

of $E'(\psi)$ in X . The resulting X Sobolev gradient $\nabla_X E(\psi) \in X$ is defined by the relation

$$(2.5) \quad (\nabla_X E(\psi), \phi)_X = \langle E'(\psi), \phi \rangle, \quad \forall \phi \in X,$$

where $\langle \cdot, \cdot \rangle$ denotes the duality pairing.

Choosing $X = L^2(\mathcal{D})$ recovers the standard L^2 gradient $\nabla_{L^2} E(\psi) = H[\psi]\psi$, which is equivalent to the imaginary time evolution method [5]. However, this approach is often hindered by numerical stiffness because $H[\psi]$ is an unbounded operator on L^2 . To mitigate this issue, we adopt an energy-adaptive metric [29, 27] induced by the bilinear form

$$(2.6) \quad a_\psi(v, w) := \int_{\mathcal{D}} \left(\frac{1}{2} \nabla v \cdot \nabla w + Vvw + \beta|\psi|^2vw \right) d\mathbf{r},$$

defined on $H_0^1(\mathcal{D})$. The a_ψ Sobolev gradient $\nabla_{a_\psi} E(\psi) \in H_0^1(\mathcal{D})$ is the solution satisfying $a_\psi(\nabla_{a_\psi} E(\psi), \phi) = \langle E'(\psi), \phi \rangle$ for all $\phi \in H_0^1(\mathcal{D})$. This metric incorporates leading-order curvature information of the energy functional and acts as a nonlinear, state-dependent preconditioner that significantly reduces the stiffness inherent in the L^2 flow.

Since the normalization constraint is defined in the L^2 geometry, the projection of an X gradient onto $T_\psi \mathbb{S}$ requires the X Riesz representer $n_\psi \in X$ of the constraint differential, satisfying $(n_\psi, \phi)_X = (\psi, \phi)_{L^2}$ for all $\phi \in X$. The Riemannian projection is defined as

$$(2.7) \quad \text{grad}_X E(\psi) = P_{\psi, X}(\nabla_X E(\psi)) = \nabla_X E(\psi) - \frac{(\nabla_X E(\psi), n_\psi)_X}{\|n_\psi\|_X^2} n_\psi.$$

The continuous projected Sobolev gradient flow is then given by

$$(2.8) \quad \partial_t \psi(t) = -\text{grad}_X E(\psi(t)),$$

which ensures both the preservation of the mass $\|\psi(t)\|_{L^2}^2 \equiv 1$ and monotonic energy dissipation.

Remark 2.1. Beyond formulations based on first-order ordinary differential equations (ODEs), various alternative computational strategies exist for obtaining BEC ground states. These include second-order ODE systems analogous to Nesterov momentum [11], Riemannian conjugate gradient methods [16], and preconditioned normalized L^2 flows [2]. While these approaches differ in terms of implementation complexity and convergence characteristics, each could potentially serve as a basis for deriving discrete neural schemes similar to the one developed here.

3. Neural discretization and natural gradient descent. This section introduces the neural network discretization of the GPE. By invoking the DFVP, we project the continuous Sobolev gradient flow onto the parameterized manifold, which yields a natural gradient evolution for the network parameters. We first detail the neural network architecture and normalization strategies before deriving the discrete parameter-space dynamics.

3.1. Deep neural network ansatz and normalization. Since the ground state wavefunction can be assumed real-valued, we employ a standard multilayer

perceptron (MLP) to parameterize the mapping $\psi_{\boldsymbol{\theta}} : \mathbb{R}^d \rightarrow \mathbb{R}$. For an input $\mathbf{r} \in \mathbb{R}^d$, the forward propagation through an L layer network follows

$$(3.1) \quad \begin{aligned} \mathbf{h}^{(0)} &= \mathbf{r}, \\ \mathbf{h}^{(l)} &= \sigma\left(\mathbf{W}^{(l)}\mathbf{h}^{(l-1)} + \mathbf{b}^{(l)}\right), \quad l = 1, \dots, L-1, \\ \psi_{\boldsymbol{\theta}}(\mathbf{r}) &= \mathbf{W}^{(L)}\mathbf{h}^{(L-1)} + \mathbf{b}^{(L)}, \end{aligned}$$

where σ denotes the activation function and $\boldsymbol{\theta} = \{\mathbf{W}^{(l)}, \mathbf{b}^{(l)}\}_{l=1}^L \in \mathbb{R}^P$ represents the set of trainable parameters.

A key challenge in learning GPE wavefunctions is enforcing the unit sphere constraint \mathbb{S} within unconstrained optimization. Standard VMC methods [48] utilize unnormalized densities by exploiting the scale invariance of linear Hamiltonians. This invariance holds not for the GPE due to its amplitude-dependent nonlinear term, necessitating strict normalization.

One solution is to impose the constraint directly via the normalized ansatz [4, 37]

$$(3.2) \quad \hat{\psi}_{\boldsymbol{\theta}}(\mathbf{r}) = \frac{\psi_{\boldsymbol{\theta}}(\mathbf{r})}{\|\psi_{\boldsymbol{\theta}}\|_{L^2(\mathcal{D})}}.$$

However, differentiating the normalization integral via automatic differentiation is computationally expensive and prone to instability. We therefore employ a hybrid approach: we use $\hat{\psi}_{\boldsymbol{\theta}}$ to ensure mass conservation but compute gradients using log-derivative statistical estimators, thus avoiding direct differentiation of the normalization factor.

3.2. Natural gradient descent. We introduce the normalized neural manifold $\mathcal{M}_{\boldsymbol{\theta}} = \{\hat{\psi}_{\boldsymbol{\theta}} \in \mathbb{S} : \boldsymbol{\theta} \in \mathbb{R}^P\}$. By the chain rule, the time derivative of $\hat{\psi}_{\boldsymbol{\theta}}$ satisfies $\partial_t \hat{\psi}_{\boldsymbol{\theta}} = \mathbf{J}(\boldsymbol{\theta})\dot{\boldsymbol{\theta}}$, where $\mathbf{J}(\boldsymbol{\theta}) = [\partial_{\theta_1} \hat{\psi}_{\boldsymbol{\theta}}, \dots, \partial_{\theta_P} \hat{\psi}_{\boldsymbol{\theta}}]$ denotes the Jacobian operator. Owing to the normalization, the parameter derivatives obey $\langle \hat{\psi}_{\boldsymbol{\theta}}, \partial_{\theta_j} \hat{\psi}_{\boldsymbol{\theta}} \rangle_{L^2} = 0$, so each $\partial_{\theta_j} \hat{\psi}_{\boldsymbol{\theta}}$ lies in the tangent space $T_{\hat{\psi}_{\boldsymbol{\theta}}} \mathbb{S}$. The parameter-induced tangent subspace is therefore

$$\mathcal{V}_{\boldsymbol{\theta}} = \text{span}\{\partial_{\theta_j} \hat{\psi}_{\boldsymbol{\theta}} : j = 1, \dots, P\} \subset T_{\hat{\psi}_{\boldsymbol{\theta}}} \mathbb{S}.$$

Since the neural ansatz possesses finite expressivity, the exact Riemannian gradient $\text{grad}_X E(\hat{\psi}_{\boldsymbol{\theta}})$ generally extends beyond the tangent subspace $\mathcal{V}_{\boldsymbol{\theta}}$. The DFVP [20, 24] resolves this by seeking a velocity $\dot{\boldsymbol{\theta}}$ whose dynamical residual is orthogonal to $\mathcal{V}_{\boldsymbol{\theta}}$ under the X -metric. This approach, also known as the Galerkin projection [8, 3], yields

$$(3.3) \quad \langle \mathbf{J}(\boldsymbol{\theta})\dot{\boldsymbol{\theta}} + \text{grad}_X E(\hat{\psi}_{\boldsymbol{\theta}}), \partial_{\theta_j} \hat{\psi}_{\boldsymbol{\theta}} \rangle_X = 0, \quad j = 1, \dots, P.$$

Expanding the above equation leads to a system of ODEs governing the evolution of the parameters

$$\sum_{i=1}^P \dot{\theta}_i (\partial_{\theta_i} \hat{\psi}_{\boldsymbol{\theta}}, \partial_{\theta_j} \hat{\psi}_{\boldsymbol{\theta}})_X = -(\text{grad}_X E(\hat{\psi}_{\boldsymbol{\theta}}), \partial_{\theta_j} \hat{\psi}_{\boldsymbol{\theta}})_X, \quad j = 1, \dots, P.$$

To simplify notation, we introduce the Gram matrix associated with the parameterized manifold $\mathcal{M}_{\boldsymbol{\theta}}$,

$$(3.4) \quad \mathbf{G}_{ij}(\boldsymbol{\theta}) = (\partial_{\theta_i} \hat{\psi}_{\boldsymbol{\theta}}, \partial_{\theta_j} \hat{\psi}_{\boldsymbol{\theta}})_X,$$

which is symmetric and positive semidefinite. Invoking the definition of the Sobolev gradient in (2.5) and using the fact that $\partial_{\theta_j} \hat{\psi}_{\theta}$ lies in the tangent space of the constraint manifold, the right-hand side can be expressed entirely in terms of derivatives with respect to the parameters. Specifically, we obtain

$$\begin{aligned} (\text{grad}_X E(\hat{\psi}_{\theta}), \partial_{\theta_j} \hat{\psi}_{\theta})_X &= (\nabla_X E(\hat{\psi}_{\theta}), \partial_{\theta_j} \hat{\psi}_{\theta})_X \\ &= \langle E'(\hat{\psi}_{\theta}), \partial_{\theta_j} \hat{\psi}_{\theta} \rangle = \frac{\partial}{\partial \theta_j} E(\hat{\psi}_{\theta}) = \nabla_{\theta} L(\theta)_j, \end{aligned}$$

where we have defined the parameter-space objective function as $L(\theta) := E(\hat{\psi}_{\theta})$. Therefore, the evolution of the parameters is governed by the natural gradient flow

$$(3.5) \quad \mathbf{G}(\theta) \dot{\theta} = -\nabla_{\theta} L(\theta),$$

which constitutes a finite-dimensional realization of the Sobolev gradient flow on the neural network manifold.

Applying the forward Euler method to (3.5) leads to the following NGD iteration

$$(3.6) \quad \theta^{k+1} = \theta^k - \tau_k \mathbf{G}(\theta^k)^{-1} \nabla_{\theta} L(\theta^k),$$

where $\tau_k > 0$ denotes the learning rate. [Figure 1](#) illustrates both the algebraic structure and the geometric interpretation of the proposed method. Panel (a) depicts a commutative diagram emphasizing manifold consistency: the discrete NGD update on Θ represents the optimal finite-dimensional approximation of the continuous Sobolev gradient flow in \mathbb{S} . Panel (b) geometrically interprets the DFVP-induced Galerkin projection \mathcal{P} . Here, the NGD update identifies the descent direction within the tangent space $T_{\hat{\psi}} \mathcal{M}_{\theta}$ that minimizes the angular deviation from the true Sobolev gradient under the X -inner product.

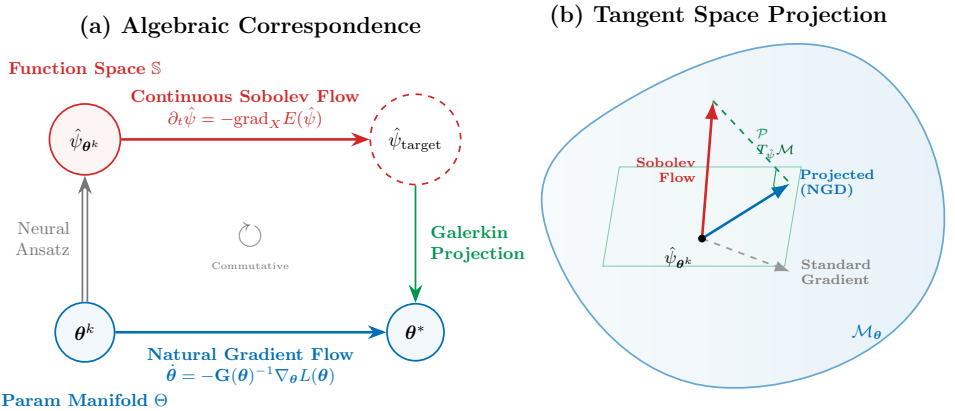


Fig. 1: Schematic of Projected Sobolev NGD method. (a) Commutative diagram relating the continuous function-space flow to the discrete parameter update. (b) Galerkin projection of the Sobolev flow onto the neural tangent space.

The choice of inner product on X dictates the structural and numerical properties of the Gram matrix $\mathbf{G}(\theta)$. While the standard L^2 metric yields the classical

Fisher information matrix—recovering the stochastic reconfiguration method [51]—it often induces numerical stiffness that necessitates Runge–Kutta schemes or specialized integrators [21, 8]. In contrast, we adopt the energy-adaptive a_ψ -inner product to define the metric. This formulation significantly mitigates the stiffness of the gradient flow, permitting stable explicit integration with large time steps of order $\mathcal{O}(1)$, cf. (5.5). The subsequent section details efficient strategies for preconditioning the inverse metric $\mathbf{G}(\boldsymbol{\theta}^k)^{-1}$ and the gradient $\nabla_{\boldsymbol{\theta}} L(\boldsymbol{\theta}^k)$.

4. Implementation via variational Monte Carlo. This section describes the practical implementation of the proposed method, focusing on the computation of the loss function $L(\boldsymbol{\theta}) = E(\hat{\psi}_{\boldsymbol{\theta}})$, its parameter gradient $\nabla_{\boldsymbol{\theta}} L(\boldsymbol{\theta})$, and the Gram matrix $\mathbf{G}(\boldsymbol{\theta})$. We first show how the energy functional and its gradient can be estimated efficiently within a VMC framework using MCMC sampling. We then introduce a hybrid sampling strategy designed to evaluate the normalization constant. Finally, we discuss the computation and preconditioning of the Gram matrix.

4.1. Estimation of the energy functional. Recall that the loss function is defined as the Gross–Pitaevskii energy evaluated at the normalized neural wavefunction $\hat{\psi}_{\boldsymbol{\theta}}$, namely

$$(4.1) \quad L(\boldsymbol{\theta}) = E(\hat{\psi}_{\boldsymbol{\theta}}) = \int_{\mathcal{D}} \left(\frac{1}{2} |\nabla \hat{\psi}_{\boldsymbol{\theta}}|^2 + V(\mathbf{r}) |\hat{\psi}_{\boldsymbol{\theta}}|^2 + \frac{\beta}{2} |\hat{\psi}_{\boldsymbol{\theta}}|^4 \right) d\mathbf{r}.$$

Let us define the normalization constant (or partition function)

$$(4.2) \quad Z(\boldsymbol{\theta}) = \|\psi_{\boldsymbol{\theta}}\|_{L^2(\mathcal{D})}^2 = \int_{\mathcal{D}} |\psi_{\boldsymbol{\theta}}(\mathbf{r})|^2 d\mathbf{r}.$$

Within the VMC framework, integrals over \mathcal{D} are reformulated as expectations with respect to the density $p_{\boldsymbol{\theta}}(\mathbf{r}) = |\hat{\psi}_{\boldsymbol{\theta}}(\mathbf{r})|^2$.

We decompose the total energy into linear and nonlinear components. The linear energy E_{lin} encompasses the kinetic and external potential terms. By introducing the local energy $E_L(\mathbf{r}; \boldsymbol{\theta}) = \hat{\psi}_{\boldsymbol{\theta}}^{-1}(-\frac{1}{2}\nabla^2 + V)\hat{\psi}_{\boldsymbol{\theta}}$, it takes the expectation form

$$(4.3) \quad E_{\text{lin}} = \int_{\mathcal{D}} \hat{\psi}_{\boldsymbol{\theta}} \left(-\frac{1}{2} \nabla^2 + V \right) \hat{\psi}_{\boldsymbol{\theta}} d\mathbf{r} = \mathbb{E}_{\mathbf{r} \sim p_{\boldsymbol{\theta}}} [E_L(\mathbf{r}; \boldsymbol{\theta})].$$

Notably, E_{lin} is invariant under the rescaling of $\psi_{\boldsymbol{\theta}}$, so $Z(\boldsymbol{\theta})$ cancels out. In contrast, the nonlinear interaction energy E_{int} explicitly depends on the amplitude

$$(4.4) \quad E_{\text{int}} = \frac{\beta}{2} \int_{\mathcal{D}} |\hat{\psi}_{\boldsymbol{\theta}}|^4 d\mathbf{r} = \mathbb{E}_{\mathbf{r} \sim p_{\boldsymbol{\theta}}} \left[\frac{\beta}{2Z(\boldsymbol{\theta})} |\psi_{\boldsymbol{\theta}}(\mathbf{r})|^2 \right].$$

Combining these contributions yields the total energy expectation

$$(4.5) \quad L(\boldsymbol{\theta}) = \mathbb{E}_{\mathbf{r} \sim p_{\boldsymbol{\theta}}} \left[E_L(\mathbf{r}; \boldsymbol{\theta}) + \frac{\beta}{2Z(\boldsymbol{\theta})} |\psi_{\boldsymbol{\theta}}(\mathbf{r})|^2 \right].$$

This formulation highlights that a stable evaluation of the scalar $Z(\boldsymbol{\theta})$ is essential. In [Subsection 4.3](#), we describe a hybrid sampling strategy designed to compute $Z(\boldsymbol{\theta})$ effectively.

4.2. Estimation of the gradients. To estimate the gradient $\nabla_{\boldsymbol{\theta}} L(\boldsymbol{\theta})$, we employ the log-derivative identity $\nabla_{\boldsymbol{\theta}} |\psi_{\boldsymbol{\theta}}|^2 = 2|\psi_{\boldsymbol{\theta}}|^2 \mathbf{O}_{\boldsymbol{\theta}}$, where $\mathbf{O}_{\boldsymbol{\theta}}(\mathbf{r}) = \nabla_{\boldsymbol{\theta}} \ln |\psi_{\boldsymbol{\theta}}(\mathbf{r})|$ denotes the score function. Differentiating the linear Rayleigh quotient E_{lin} and the nonlinear interaction energy E_{int} with respect to $\boldsymbol{\theta}$, and applying the quotient rule to handle the normalization factor $Z(\boldsymbol{\theta})$, allows us to express the total gradient as an expectation over the probability density $p_{\boldsymbol{\theta}}$.

To present the estimator in a concise form, we introduce the *local chemical potential* $\mu_L(\mathbf{r})$, which effectively aggregates the local energy and the potential induced by the nonlinearity

$$(4.6) \quad \mu_L(\mathbf{r}) := E_L(\mathbf{r}) + \frac{\beta}{Z(\boldsymbol{\theta})} |\psi_{\boldsymbol{\theta}}(\mathbf{r})|^2.$$

Correspondingly, we denote the mean chemical potential as $\bar{\mu} = \mathbb{E}_{\mathbf{r} \sim p_{\boldsymbol{\theta}}} [\mu_L(\mathbf{r})]$, noting that $\bar{\mu} = E_{\text{lin}} + 2E_{\text{int}}$ due to the scaling of the interaction term. Combining these definitions, the gradient of the loss function is given by

$$(4.7) \quad \nabla_{\boldsymbol{\theta}} L(\boldsymbol{\theta}) = 2 \mathbb{E}_{\mathbf{r} \sim p_{\boldsymbol{\theta}}} [(\mu_L(\mathbf{r}) - \bar{\mu}) \mathbf{O}_{\boldsymbol{\theta}}(\mathbf{r})].$$

This estimator, structured as a covariance between the local chemical potential and the score function, inherently acts as a control variate formulation, reducing the variance of the stochastic gradients.

4.3. Hybrid sampling strategy. The explicit dependence of the energy expectation (4.5) on the normalization constant $Z(\boldsymbol{\theta})$ necessitates a dual sampling approach. We employ a hybrid strategy comprising two distinct routines:

Gradient Estimation: The first routine estimates energy gradients via MCMC sampling (e.g., Metropolis–Hastings (M-H) [42] or Hamiltonian Monte Carlo (HMC) [43]) from $p_{\boldsymbol{\theta}}$. By concentrating samples in high-probability regions where $|\hat{\psi}_{\boldsymbol{\theta}}|^2$ is large, this method yields low-variance estimators efficiently.

Normalization via ADIS: The second routine computes $Z(\boldsymbol{\theta})$ using Monte Carlo integration to overcome the curse of dimensionality inherent in grid-based quadrature. We utilize an adaptive defensive importance sampling (ADIS) strategy, expressing the constant as $Z(\boldsymbol{\theta}) = \mathbb{E}_{\mathbf{r} \sim q} [|\psi_{\boldsymbol{\theta}}|^2 / q]$. The proposal q is a mixture

$$(4.8) \quad q(\mathbf{r}) = \alpha q_{\mathcal{N}}(\mathbf{r} \mid \boldsymbol{\mu}, \boldsymbol{\Sigma}) + (1 - \alpha) q_{\mathcal{U}}(\mathbf{r} \mid \Omega), \quad \alpha \in [0, 1].$$

Here, $q_{\mathcal{N}}$ is a multivariate Gaussian updated using statistics from the MCMC stream to track the wavefunction’s mass, while the defensive uniform component $q_{\mathcal{U}}$ guarantees global support. This combination prevents variance explosion and ensures the method scales linearly with sample size, independent of spatial dimension.

4.4. Computation of the Gram matrix. We adopt the $a_{\hat{\psi}}$ -inner product evaluated at the normalized wavefunction $\hat{\psi}_{\boldsymbol{\theta}}$ as the underlying metric for constructing the Gram matrix, cf. (2.6). Specifically, the bilinear form is defined as

$$(4.9) \quad a_{\hat{\psi}}(u, v) = \int_{\mathcal{D}} \left(\frac{1}{2} \nabla u \cdot \nabla v + V(\mathbf{r}) uv + \frac{\beta}{Z(\boldsymbol{\theta})} |\psi_{\boldsymbol{\theta}}(\mathbf{r})|^2 uv \right) d\mathbf{r},$$

The Gram matrix is then given by

$$(4.10) \quad \mathbf{G}_{ij}(\boldsymbol{\theta}) = a_{\hat{\psi}} \left(\frac{\partial \hat{\psi}_{\boldsymbol{\theta}}}{\partial \theta_i}, \frac{\partial \hat{\psi}_{\boldsymbol{\theta}}}{\partial \theta_j} \right).$$

We first derive an explicit expression for the tangent vectors associated with the normalized wavefunction $\hat{\psi}_{\boldsymbol{\theta}} = \psi_{\boldsymbol{\theta}}/\sqrt{Z(\boldsymbol{\theta})}$. Differentiating with respect to a parameter θ_k yields

$$(4.11) \quad \begin{aligned} \frac{\partial \hat{\psi}_{\boldsymbol{\theta}}}{\partial \theta_k} &= \frac{\partial}{\partial \theta_k} \left(\frac{\psi_{\boldsymbol{\theta}}}{\sqrt{Z}} \right) = \frac{(\partial_{\theta_k} \psi_{\boldsymbol{\theta}}) \sqrt{Z} - \psi_{\boldsymbol{\theta}} \left(\frac{1}{2\sqrt{Z}} \partial_{\theta_k} Z \right)}{Z} \\ &= \hat{\psi}_{\boldsymbol{\theta}} \left(\frac{\partial_{\theta_k} \psi_{\boldsymbol{\theta}}}{\psi_{\boldsymbol{\theta}}} - \frac{1}{2} \frac{\partial_{\theta_k} Z}{Z} \right). \end{aligned}$$

Introducing the log-derivative $\mathbf{O}_k(\mathbf{r}) := \partial_{\theta_k} \ln |\psi_{\boldsymbol{\theta}}(\mathbf{r})|$, and recalling that $\partial_{\theta_k} Z = 2Z \mathbb{E}_{\mathbf{r} \sim p_{\boldsymbol{\theta}}} [\mathbf{O}_k]$, we arrive at the compact form

$$(4.12) \quad \frac{\partial \hat{\psi}_{\boldsymbol{\theta}}}{\partial \theta_k} = \hat{\psi}_{\boldsymbol{\theta}}(\mathbf{r}) (\mathbf{O}_k(\mathbf{r}) - \mathbb{E}_{\mathbf{r} \sim p_{\boldsymbol{\theta}}} [\mathbf{O}_k]) =: \hat{\psi}_{\boldsymbol{\theta}}(\mathbf{r}) \delta \mathbf{O}_k(\mathbf{r}),$$

where $\delta \mathbf{O}_k$ denotes the *centered score function*, satisfying $\mathbb{E}_{p_{\boldsymbol{\theta}}} [\delta \mathbf{O}_k] = 0$. This centering reflects the orthogonality of tangent vectors to the normalization constraint.

4.4.1. Gradient expansion of the kinetic term. We now evaluate the kinetic contribution

$$\frac{1}{2} \nabla (\partial_{\theta_i} \hat{\psi}_{\boldsymbol{\theta}}) \cdot \nabla (\partial_{\theta_j} \hat{\psi}_{\boldsymbol{\theta}}).$$

Using (4.12) and the product rule,

$$(4.13) \quad \nabla \left(\hat{\psi}_{\boldsymbol{\theta}} \delta \mathbf{O}_k \right) = (\nabla \hat{\psi}_{\boldsymbol{\theta}}) \delta \mathbf{O}_k + \hat{\psi}_{\boldsymbol{\theta}} \nabla \delta \mathbf{O}_k.$$

Define the *quantum force* $\mathbf{F}(\mathbf{r}) := \nabla \ln |\hat{\psi}_{\boldsymbol{\theta}}(\mathbf{r})| = \frac{\nabla \hat{\psi}_{\boldsymbol{\theta}}}{\hat{\psi}_{\boldsymbol{\theta}}}$. Since $\delta \mathbf{O}_k = \mathbf{O}_k - \mathbb{E}[\mathbf{O}_k]$, its gradient satisfies $\nabla \delta \mathbf{O}_k = \nabla \mathbf{O}_k$. Therefore,

$$(4.14) \quad \nabla \left(\frac{\partial \hat{\psi}_{\boldsymbol{\theta}}}{\partial \theta_k} \right) = \hat{\psi}_{\boldsymbol{\theta}}(\mathbf{r}) (\mathbf{F}(\mathbf{r}) \delta \mathbf{O}_k(\mathbf{r}) + \nabla \mathbf{O}_k(\mathbf{r})).$$

Substituting the expressions for indices i and j into the kinetic term yields

$$(4.15) \quad \begin{aligned} \mathbf{K}_{ij} &= \int_{\mathcal{D}} \frac{1}{2} \left[\hat{\psi}_{\boldsymbol{\theta}} (\mathbf{F} \delta \mathbf{O}_i + \nabla \mathbf{O}_i) \right] \cdot \left[\hat{\psi}_{\boldsymbol{\theta}} (\mathbf{F} \delta \mathbf{O}_j + \nabla \mathbf{O}_j) \right] \mathrm{d}\mathbf{r} \\ &= \int_{\mathcal{D}} \frac{1}{2} |\hat{\psi}_{\boldsymbol{\theta}}|^2 \left[|\mathbf{F}|^2 \delta \mathbf{O}_i \delta \mathbf{O}_j + \mathbf{F} \cdot (\delta \mathbf{O}_i \nabla \mathbf{O}_j + \delta \mathbf{O}_j \nabla \mathbf{O}_i) + \nabla \mathbf{O}_i \cdot \nabla \mathbf{O}_j \right] \mathrm{d}\mathbf{r} \\ &= \mathbb{E}_{\mathbf{r} \sim p_{\boldsymbol{\theta}}} \left[\frac{1}{2} |\mathbf{F}|^2 \delta \mathbf{O}_i \delta \mathbf{O}_j + \frac{1}{2} \mathbf{F} \cdot (\delta \mathbf{O}_i \nabla \mathbf{O}_j + \delta \mathbf{O}_j \nabla \mathbf{O}_i) + \frac{1}{2} \nabla \mathbf{O}_i \cdot \nabla \mathbf{O}_j \right], \end{aligned}$$

where we have used $p_{\boldsymbol{\theta}} = |\hat{\psi}_{\boldsymbol{\theta}}|^2$ to convert the integral into an expectation.

4.4.2. Potential and interaction terms. Substituting the tangent vectors $\hat{\psi}_{\boldsymbol{\theta}} \delta \mathbf{O}_k$ directly, we obtain

$$(4.16) \quad \begin{aligned} \mathbf{V}_{ij} + \mathbf{I}_{ij} &= \int_{\mathcal{D}} \left(V(\mathbf{r}) + \frac{\beta}{Z(\boldsymbol{\theta})} |\psi_{\boldsymbol{\theta}}(\mathbf{r})|^2 \right) (\hat{\psi}_{\boldsymbol{\theta}} \delta \mathbf{O}_i)(\hat{\psi}_{\boldsymbol{\theta}} \delta \mathbf{O}_j) \mathrm{d}\mathbf{r} \\ &= \mathbb{E}_{\mathbf{r} \sim p_{\boldsymbol{\theta}}} \left[\left(V(\mathbf{r}) + \frac{\beta}{Z(\boldsymbol{\theta})} |\psi_{\boldsymbol{\theta}}(\mathbf{r})|^2 \right) \delta \mathbf{O}_i(\mathbf{r}) \delta \mathbf{O}_j(\mathbf{r}) \right]. \end{aligned}$$

Collecting (4.15) and (4.16), it is convenient to group all coefficients multiplying $\delta\mathbf{O}_i\delta\mathbf{O}_j$ into a single weight function, termed the *generalized energy density*

$$(4.17) \quad \mathcal{W}(\mathbf{r}) = V(\mathbf{r}) + \frac{\beta}{Z(\boldsymbol{\theta})} |\psi_{\boldsymbol{\theta}}(\mathbf{r})|^2 + \frac{1}{2} |\mathbf{F}(\mathbf{r})|^2.$$

The Sobolev Gram matrix then admits the compact expectation form

$$(4.18) \quad \begin{aligned} \mathbf{G}_{ij}(\boldsymbol{\theta}) &= \mathbb{E}_{\mathbf{r} \sim p_{\boldsymbol{\theta}}} \left[\underbrace{\mathcal{W}(\mathbf{r}) \delta\mathbf{O}_i(\mathbf{r}) \delta\mathbf{O}_j(\mathbf{r})}_{\text{Term I: energy-weighted Fisher information}} \right. \\ &\quad + \underbrace{\frac{1}{2} \mathbf{F}(\mathbf{r}) \cdot (\nabla\mathbf{O}_i(\mathbf{r}) \delta\mathbf{O}_j(\mathbf{r}) + \nabla\mathbf{O}_j(\mathbf{r}) \delta\mathbf{O}_i(\mathbf{r}))}_{\text{Term II: drift-gradient coupling}} \\ &\quad \left. + \underbrace{\frac{1}{2} \nabla\mathbf{O}_i(\mathbf{r}) \cdot \nabla\mathbf{O}_j(\mathbf{r})}_{\text{Term III: pure Sobolev regularization}} \right]. \end{aligned}$$

4.5. Matrix-free PCG solver based on Nyström preconditioning. Since the Gram matrix $\mathbf{G}(\boldsymbol{\theta})$ is symmetric positive semidefinite, we introduce a Tikhonov regularization term $\lambda\mathbf{I}$ with $\lambda > 0$ to ensure invertibility. Projecting the Sobolev gradient flow onto the parameter space requires solving the linear system $(\mathbf{G}(\boldsymbol{\theta}) + \lambda\mathbf{I})\dot{\boldsymbol{\theta}} = -\nabla_{\boldsymbol{\theta}}L(\boldsymbol{\theta})$. For modern deep neural network architectures, the parameter dimension P often exceeds 10^5 , which makes the explicit formation of the Gram matrix or its direct inversion computationally prohibitive due to the quadratic memory cost and cubic time complexity. To address this limitation, we adopt a matrix-free preconditioned conjugate gradient (PCG) solver that only requires matrix-vector products of the form $\mathbf{v} \mapsto \mathbf{G}\mathbf{v}$.

4.5.1. Matrix-free implementation. The implementation follows a Jacobian-based matrix-free paradigm consistent with the Sobolev Gram matrix definition (4.18). Although the full matrix $\mathbf{G}(\boldsymbol{\theta})$ is never assembled, its action on an arbitrary vector $\mathbf{v} \in \mathbb{R}^P$ can be evaluated exactly through batched contractions. For a set of Monte Carlo samples $\{\mathbf{r}_n\}_{n=1}^N$, we define the Jacobian tensor $\mathbf{J} \in \mathbb{R}^{N \times P}$ with entries $\mathbf{J}_{n,:} = \delta\mathbf{O}(\mathbf{r}_n)^T$ and the mixed-derivative tensor $\mathbf{K} \in \mathbb{R}^{N \times P \times D}$ with entries $\mathbf{K}_{n,:,d} = \nabla_{r_d}\mathbf{O}(\mathbf{r}_n)^T$. We also define the drift field $\mathbf{F}(\mathbf{r}_n) \in \mathbb{R}^D$ and the generalized energy density $\mathcal{W}(\mathbf{r}_n)$.

Using the associativity of matrix multiplication and the symmetry of \mathbf{G} , the matrix-vector product can be evaluated through three distinct contributions as follows

$$\begin{aligned} \mathbf{G}\mathbf{v} &= \frac{1}{N} \left[\mathbf{J}^T (\mathbf{W} \odot (\mathbf{J}\mathbf{v})) + \frac{1}{2} \sum_{d=1}^D \left(\mathbf{K}_{:,,:,d}^T (\mathbf{F}_{:,d} \odot (\mathbf{J}\mathbf{v})) + \mathbf{J}^T (\mathbf{F}_{:,d} \odot (\mathbf{K}_{:,,:,d}\mathbf{v})) \right) \right. \\ &\quad \left. + \frac{1}{2} \sum_{d=1}^D \mathbf{K}_{:,,:,d}^T (\mathbf{K}_{:,,:,d}\mathbf{v}) \right], \end{aligned}$$

where $\mathbf{W} \in \mathbb{R}^N$ is a vector of the generalized energy densities and \odot denotes elementwise multiplication.

4.5.2. Randomized Nyström preconditioning. To accelerate the convergence of the PCG solver, we utilize a low-rank approximation of the Gram matrix through a randomized Nyström method [23]. We approximate the matrix as

$\mathbf{G} \approx \mathbf{M}\mathbf{M}^\top$, where $\mathbf{M} \in \mathbb{R}^{P \times r}$ with $r \ll P$. The construction follows a GPU-efficient Nyström approximation technique [26]:

1. Generate a Gaussian random test matrix $\boldsymbol{\Omega} \in \mathbb{R}^{P \times r}$;
2. Compute the projected matrix $\mathbf{Y} = \mathbf{G}\boldsymbol{\Omega}$ using the matrix-free $\mathbf{G}\mathbf{v}$ operator;
3. Form the Nyström basis

$$\mathbf{M} = \mathbf{Y}(\boldsymbol{\Omega}^\top \mathbf{Y} + \varepsilon \mathbf{I})^{-1/2},$$

where a small shift $\varepsilon > 0$ is added for numerical stability.

By applying the Woodbury matrix identity, the inverse of the preconditioned system can be expressed in a closed form that is efficient to compute

$$(4.19) \quad (\mathbf{M}\mathbf{M}^\top + \lambda \mathbf{I})^{-1} = \frac{1}{\lambda} \left[\mathbf{I} - \mathbf{M} (\mathbf{M}^\top \mathbf{M} + \lambda \mathbf{I}_r)^{-1} \mathbf{M}^\top \right].$$

This formulation reduces the inversion cost to the order of Pr^2 , which is computationally tractable for moderate ranks such as $r = 128$. To further enhance efficiency, we implement a lazy update strategy where the Nyström basis is refreshed only every fixed number of training iterations, such as every ten steps, thereby significantly reducing the overall computational overhead.

4.6. More implementation details. Algorithm 4.1 outlines the comprehensive workflow of the proposed Sobolev NGD method. To ensure robustness, efficiency, and scalability, we incorporate several specialized techniques into the numerical implementation.

For example, we integrate an adaptive damping strategy to stabilize the inversion of the Gram matrix. Inspired by the Levenberg–Marquardt scheme [40], we dynamically adjust the damping parameter based on the observed change in the energy functional, cf. (5.6). A significant reduction in energy allows for a decrease in λ to facilitate more aggressive steps, while any increase in energy triggers a sharp increase in damping to preserve numerical stability and ensure monotonic convergence. To overcome the spectral bias inherent in standard MLP architectures, we augment the spatial coordinates with Gaussian random Fourier features [52]. Mapping the input \mathbf{r} to the embedding $\gamma(\mathbf{r}) = [\cos(2\pi\mathbf{Br}), \sin(2\pi\mathbf{Br})]$ enables the network to represent high-frequency spatial structures that would otherwise be difficult to resolve.

5. Numerical experiments. This section presents a systematic numerical investigation of the proposed method. The experiments cover a variety of multi-scale physical settings, ranging from low-dimensional problems with strongly nonlinear optical lattice potentials to higher-dimensional systems with fully coupled anisotropic harmonic confinement, thereby assessing the scalability of the method with respect to spatial dimension.

5.1. Experimental setup and evaluation metrics. To quantitatively assess the accuracy of the neural wavefunction $\hat{\psi}_\theta$ for the nonlinear GPE, we adopt the variance of the local chemical potential (hereafter referred to as the *local variance*) as the primary convergence and accuracy indicator. For normalized wavefunctions, this quantity is equivalent to the squared residual norm of the nonlinear eigenvalue problem and can be expressed as

$$(5.1) \quad \begin{aligned} \text{Res}(\hat{\psi}) &= \|H[\hat{\psi}]\hat{\psi} - \mu_1 \hat{\psi}\|_2^2 = \int |\hat{\psi}(\mathbf{r})|^2 \left| \frac{H[\hat{\psi}]\hat{\psi}(\mathbf{r})}{\hat{\psi}(\mathbf{r})} - \mu_1 \right|^2 d\mathbf{r} \\ &= \mathbb{E}_{\mathbf{r} \sim |\hat{\psi}|^2} \left[(\mu_L(\mathbf{r}) - \mu_1)^2 \right] = \text{Var}_{\mathbf{r} \sim |\hat{\psi}|^2} [\mu_L(\mathbf{r})]. \end{aligned}$$

Algorithm 4.1 Projected Sobolev NGD for the GPE

Require: Initial parameters θ_0 , learning rate τ_k , damping λ_k , Nyström rank $r = 128$, update frequency $K = 10$.

Ensure: Ground state wavefunction approximation $\hat{\psi}_\theta$.

- 1: **Initialization:** Run MCMC walkers $\mathcal{X}_{\text{mcmc}}$.
- 2: **for** $k = 0, 1, 2, \dots$ until convergence **do**
- 3: **Step 1: Hybrid Sampling and Statistics**
- 4: Update walkers $\mathcal{X}_{\text{mcmc}} = \{\mathbf{r}_n\}_{n=1}^N$ via MCMC sampling from $p_\theta(\mathbf{r}) \propto |\psi_\theta(\mathbf{r})|^2$.
- 5: Compute stats (μ, Σ) from $\mathcal{X}_{\text{mcmc}}$ and update the ADIS proposal $q(\mathbf{r})$.
- 6: Estimate normalization constant $Z(\theta)$ using ADIS samples \mathcal{X}_{int} .
- 7: **Step 2: Gradient Estimation**
- 8: Evaluate local chemical potential $\mu_L(\mathbf{r}_n) = E_L(\mathbf{r}_n) + \frac{\beta}{Z(\theta)} |\psi_\theta(\mathbf{r}_n)|^2$.
- 9: Estimate loss gradient $\mathbf{g}_k = \frac{2}{N} \sum_{n=1}^N (\mu_L(\mathbf{r}_n) - \bar{\mu}) \nabla_\theta \ln |\psi_\theta(\mathbf{r}_n)|$.
- 10: **Step 3: Randomized Nyström Preconditioner (Lazy Update)**
- 11: **if** $k \pmod{K} == 0$ **then**
- 12: Generate Gaussian random matrix $\Omega \in \mathbb{R}^{P \times r}$.
- 13: Compute $\mathbf{Y} = \mathbf{G}\Omega$ via matrix-free operator.
- 14: Form Nyström basis $\mathbf{M} = \mathbf{Y}(\Omega^\top \mathbf{Y} + \varepsilon \mathbf{I})^{-1/2}$.
- 15: **end if**
- 16: **Step 4: Natural Gradient Direction Search**
- 17: Solve $(\mathbf{G} + \lambda_k \mathbf{I}) \dot{\theta}_k = -\mathbf{g}_k$ using matrix-free PCG.
- 18: Apply preconditioning via the Woodbury identity:
- 19:
$$P^{-1} \mathbf{v} = \frac{1}{\lambda_k} \left[\mathbf{v} - \mathbf{M} \left(\mathbf{M}^\top \mathbf{M} + \lambda_k \mathbf{I}_r \right)^{-1} \mathbf{M}^\top \mathbf{v} \right].$$
- 20: **Step 5: Parameter and Damping Update**
- 21: Update parameters: $\theta_{k+1} = \theta_k + \tau_k \dot{\theta}_k$.
- 22: Adjust damping λ_k according to energy reduction.
- 23: **end for**
- 24: **return** $\hat{\psi}_\theta = \psi_\theta / \sqrt{Z(\theta)}$

For low-dimensional problems (2D and 3D), further validation is performed by comparison with high-accuracy reference solutions computed using the DFTK.jl package [30], which is based on direct energy minimization with plane-wave basis sets. The following relative error metrics are reported

$$(5.2) \quad \varepsilon_E = \frac{|E_{\text{NN}} - E_{\text{ref}}|}{|E_{\text{ref}}|}, \quad (\text{relative energy error}),$$

$$(5.3) \quad \varepsilon_\mu = \frac{|\mu_{\text{NN}}^{\text{NN}} - \mu_{\text{ref}}|}{|\mu_{\text{ref}}|}, \quad (\text{relative chemical potential error}),$$

$$(5.4) \quad \varepsilon_\rho = \frac{\|\rho_{\text{NN}} - \rho_{\text{ref}}\|_2}{\|\rho_{\text{ref}}\|_2}, \quad (\text{relative density } L^2 \text{ error}),$$

where $\rho(\mathbf{r}) = |\hat{\psi}(\mathbf{r})|^2$ denotes the probability density.

In all numerical experiments, the wavefunction is parameterized by a MLP comprising 5 hidden layers with 50 neurons each. We employ the hyperbolic tangent activation function due to its smoothness and boundedness. For the baseline optimization using Adam, we fix the learning rate at 10^{-3} . Conversely, for the proposed

NGD method, we adopt an adaptive step size

$$(5.5) \quad \tau_k = 0.5 + 0.5 \frac{\text{Res}(\hat{\psi})}{1 + \text{Res}(\hat{\psi})},$$

which accelerates early-stage descent while permitting more refined updates near convergence. Furthermore, the damping parameter is governed by

$$(5.6) \quad \lambda_k = \min(10^{-3}, 10^{-3} \text{Res}(\hat{\psi})),$$

balancing numerical stability with the incorporation of effective curvature information throughout the optimization process. Complete implementation details are available in the code repository: <https://github.com/cuichen1996/NGD4GPE>.

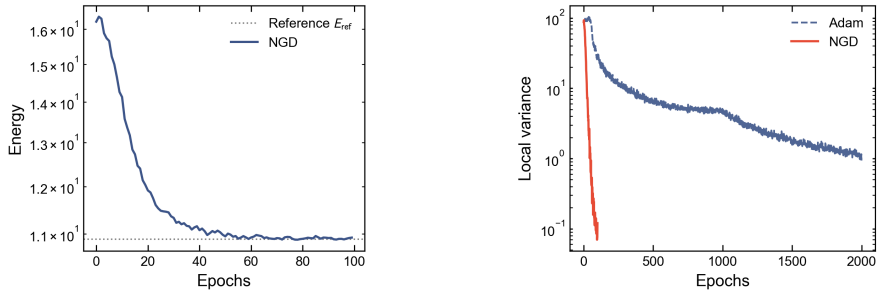
5.2. 2D optical lattice potential. We consider a 2D optical lattice with anisotropic harmonic confinement [28], defined by

$$(5.7) \quad V(x, y) = \frac{1}{4}(x^2 + 4y^2) + 5(\sin^2(\pi x) + \sin^2(\pi y)).$$

With interactions fixed at $\beta = 250$ on the domain $\mathcal{D} = [-8, 8]^2$, the ground state exhibits a multiscale structure: a macroscopic harmonic envelope modulated by high-frequency lattice oscillations.

To resolve these high-frequency features, the neural ansatz incorporates Fourier feature embeddings ($\mathbf{B} \in \mathbb{R}^{32 \times 2}$). Expectations are estimated via M-H sampling (4000 samples), while the normalization constant Z is computed on a uniform 100×100 grid. We compare the proposed NGD method (100 epochs) against the Adam optimizer (2000 epochs).

Figures 2a and 2b displays the energy evolution and the convergence of the local variance, respectively. While Adam shows rapid initial descent, it stagnates in later stages. In contrast, NGD achieves stable, monotonic convergence by exploiting the curvature information encoded in the Sobolev metric.



(a) Evolution of the ground state energy during NGD optimization.

(b) Comparison of Adam and NGD in terms of the local variance $\text{Res}(\hat{\psi})$.

Fig. 2: Convergence history for the 2D optical lattice potential.

Figure 3 visualizes the ground state density obtained by NGD. The numerical solution accurately captures both the smooth global envelope and the checkerboard-like periodic modulation induced by the lattice potential, demonstrating the ability of the proposed method to resolve features across multiple spatial scales.

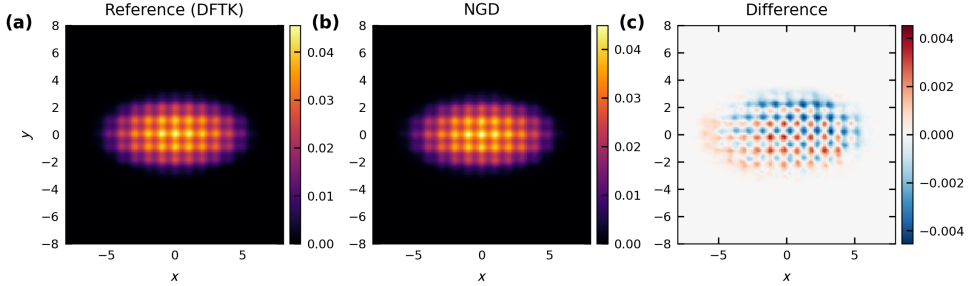


Fig. 3: Ground state density for the 2D optical lattice potential computed by NGD.

Table 1 reports the quantitative error metrics at convergence. While both optimizers attain comparable levels of accuracy, NGD requires substantially fewer iterations, highlighting its superior iteration efficiency.

Table 1: Error comparison for the 2D optical lattice potential problem.

| Optimizer | Ground State Energy E | Chemical Potential μ | Ground State Density ρ | Iter. |
|-----------|-------------------------|--------------------------|-----------------------------|-----------|
| | ε_E | ε_μ | ε_ρ | |
| Adam | 8.8×10^{-4} | 2.2×10^{-3} | 7.2×10^{-2} | 1959 |
| NGD | 4.9×10^{-3} | 9.4×10^{-3} | 6.2×10^{-2} | 74 |

Finally, **Table 2** compares the computational cost associated with different optimization and preconditioning strategies. Here, NGD (Explicit G) refers to the direct use of the full Gram matrix without preconditioning, while NGD (Block-Jacobi-PCG) employs a layer-wise block-Jacobi preconditioner, which can be interpreted as a nonoverlapping *domain decomposition preconditioner in parameter space*. NGD (Nyström-PCG) corresponds to the proposed Nyström-preconditioned approach. Although the per-iteration cost of NGD is moderately higher than that of Adam, the overall training time is substantially reduced due to the significantly faster convergence. In particular, the Nyström-PCG strategy reduces GPU memory consumption by more than an order of magnitude compared with the explicit Gram matrix approach, while simultaneously achieving an end-to-end speedup of approximately $3.6 \times$ relative to the Adam baseline. These results demonstrate that the proposed method is both computationally efficient and scalable for large-scale multiscale physical problems.

5.3. 3D optical lattice potential. To further assess the accuracy and efficiency of the proposed ADIS strategy, we consider a benchmark problem involving a 3D optical lattice potential. In this moderate-dimensional setting, deterministic quadrature based on structured grids remains computationally feasible and therefore provides a reliable reference for validating the ADIS framework. Following [4], the external trapping potential is given by

$$(5.8) \quad V(x, y, z) = \frac{1}{2}(x^2 + y^2 + z^2) + \frac{5}{2} \left(\sin^2\left(\frac{\pi x}{4}\right) + \sin^2\left(\frac{\pi y}{4}\right) + \sin^2\left(\frac{\pi z}{4}\right) \right),$$

Table 2: Comparison of computational overhead for different optimization and preconditioning strategies on an A100 GPU.

| Algorithm | ε_ρ | Epochs | Time (s) | Speedup | VRAM (GB) |
|--------------------------|--------------------|--------|-------------|-------------------------------|-----------|
| Adam (Baseline) | 7.2% | 2000 | 67.1 | 1.0 \times | 0.7 |
| NGD (Explicit G) | 6.2% | 100 | 61.9 | 1.1 \times | 25.1 |
| NGD (Block-Jacobi-PCG) | 6.3% | 100 | 23.5 | 2.8 \times | 4.1 |
| NGD (Nyström-PCG) | 6.3% | 100 | 18.7 | 3.6\times | 2.4 |

with interaction strength $\beta = 200$ and computational domain $\mathcal{D} = [-6, 6]^3$. We compare two strategies for evaluating the normalization constant Z : a deterministic Riemann sum on a uniform tensor grid with 100^3 points, and the proposed ADIS method using 8000 samples with a mixture ratio $\alpha = 0.8$.

The results in Figure 4 illustrate both the neural VMC solution and the sampling behavior induced by ADIS. Specifically, Figure 4a displays planar slices of the optimized ground state density, Figure 4b illustrates the spatial distribution of MCMC walkers during training, and Figure 4c shows the ADIS-generated samples employed for estimating Z . The close agreement between the ADIS sample distribution and the ground state density indicates that the adaptive proposal successfully concentrates samples in high-probability regions of the configuration space.

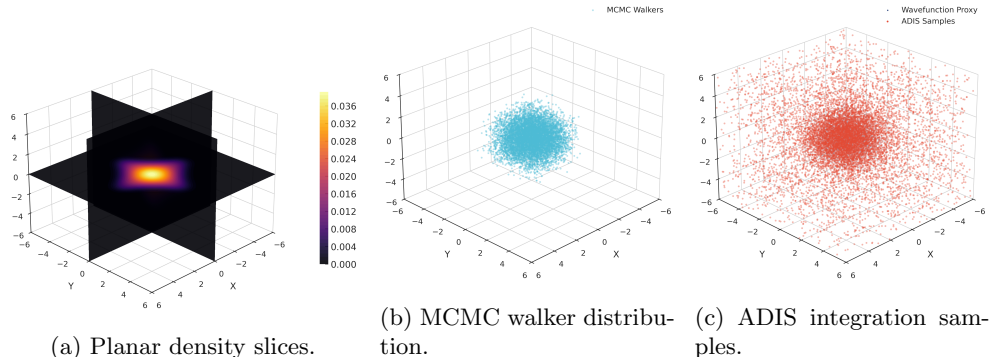


Fig. 4: Visualization of the ground state density and sampling profiles for the 3D optical lattice problem.

Table 3 reports a comparison between the two computational strategies. The results show that ADIS attains an accuracy comparable to that of the dense grid-based Riemann sum while using only approximately 1% of the total sample points. This observation is particularly significant in view of the fact that the computational cost of grid-based quadrature grows exponentially with the spatial dimension. In contrast, ADIS eliminates the reliance on full tensor grids and thereby avoids the curse of dimensionality. Although ADIS incurs a moderate memory overhead associated with constructing the adaptive proposal, it offers a scalable and practical strategy for high-dimensional problems.

Table 3: Comparison of accuracy and computational cost between deterministic grid-based integration and the ADIS framework for the 3D optical lattice problem.

| Method | Sample Points | Time (s) | ε_ρ | VRAM (GB) |
|-------------|---------------|----------|-----------------------|-----------|
| Riemann sum | 100^3 | 38.6 | 6.05×10^{-2} | 4.6 |
| ADIS | 8000 | 39.0 | 5.92×10^{-2} | 7.8 |

5.3.1. Neural network solution as an initial guess. To further improve the accuracy of the computed ground states, we adopt a hybrid strategy in which the solution obtained by NGD is used as a high-quality initial guess for a subsequent high-precision solver. Specifically, the optimized neural wavefunction is projected onto a plane-wave basis by evaluating the network on a uniform real-space grid and applying a fast Fourier transform to obtain the corresponding spectral coefficients. This spectrally represented state is then used to initialize the energy adaptive Riemannian conjugate gradient (EARCG) method [47]. In practice, we use the neural network solution obtained after only 20 NGD iterations, requiring less than 10 seconds of wall-clock time, as the initial state for the refinement stage.

As shown in Figure 5, this neural-network-warmed initialization leads to a pronounced improvement over a standard default initialization. In particular, it bypasses the initial high-energy relaxation phase and substantially reduces the initial energy error. Moreover, the subsequent EARCG iterations exhibit a significantly steeper convergence rate on a logarithmic error scale. This behavior indicates that the neural network has already captured the global structure of the ground state wavefunction and has placed the iterate within the quadratic convergence basin of the local optimizer, thereby mitigating the severe ill-conditioning typically associated with nonlinear Gross–Pitaevskii energy landscapes.

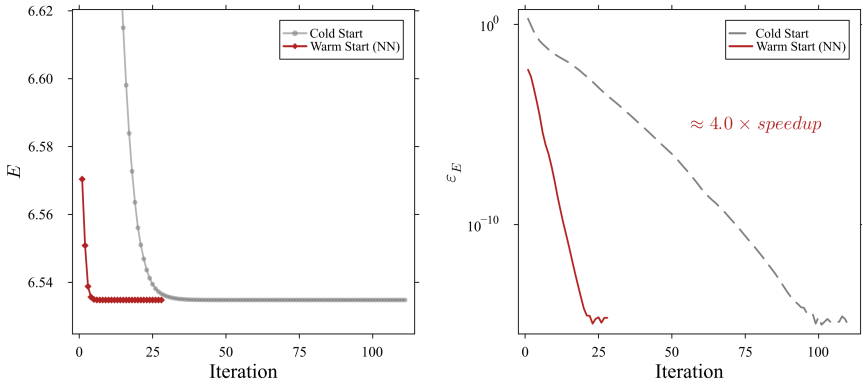


Fig. 5: Energy convergence of the EARCG solver with neural-network-warmed initialization versus a default initial guess.

5.4. Comparison with the norm-DNN. Before proceeding to higher dimensional experiments, we compare the proposed method with the recently introduced norm-DNN approach [4], which is a PINN-based method that enforces the mass con-

straint through an explicit normalization layer. In the 3D setting, norm-DNN considers the discretized optimization problem

$$(5.9) \quad \min_{\theta} \left\{ \mathcal{L} = \frac{|\mathcal{D}|}{N_b} \sum_{j,k,l} \left[\frac{1}{2} \left| \nabla \hat{\psi}_{\theta} \right|^2 + V \left| \hat{\psi}_{\theta} \right|^2 + \frac{1}{2} \beta \left| \hat{\psi}_{\theta} \right|^4 \right]_{(x_j, y_k, z_l)} \right\}.$$

We perform comparative studies on two benchmark problems reported in [4], strictly following the original experimental settings. The first example is a 2D optical lattice problem with potential

$$(5.10) \quad V(x, y) = \frac{1}{2} (x^2 + y^2) + \frac{5}{2} \left(\sin^2 \left(\frac{\pi x}{4} \right) + \sin^2 \left(\frac{\pi y}{4} \right) \right),$$

posed on the domain $\mathcal{D} = [-6, 6]^2$ with interaction strength $\beta = 400$. The second example is the 3D optical lattice problem defined by (5.8) on $\mathcal{D} = [-6, 6]^3$ with $\beta = 200$.

The results are summarized in Table 4. Overall, the proposed method exhibits a clear advantage over norm-DNN in terms of both convergence behavior and computational efficiency. In both test cases, our method converges within only 100 training epochs, whereas norm-DNN requires between 30,000 and 100,000 epochs to reach comparable accuracy. Moreover, the proposed approach demonstrates substantially improved sample efficiency. In particular, for the 3D optical lattice problem, it achieves a lower relative L^2 error in the ground state density while using significantly fewer spatial sampling points. These results highlight the effectiveness of the projected Sobolev NGD framework for challenging high-dimensional nonlinear eigenvalue problems.

Table 4: Comparison between the projected Sobolev NGD method and the Norm-DNN method [4] for 2D and 3D optical lattice benchmark problems.

| Method | Batch Size | Epochs | ε_{ρ} | ε_E | Time (s) |
|--|------------|------------|---|---|-------------|
| 2D Case (Optical Lattice, $\beta = 400$) | | | | | |
| Norm-DNN | 4096 | 30,000 | 4.82×10^{-2} | 2.08×10^{-3} | 169.7 |
| Ours | 4000 | 100 | 3.14×10^{-2} | 7.51×10^{-4} | 15.1 |
| 3D Case (Optical Lattice, $\beta = 200$) | | | | | |
| Norm-DNN | 60,000 | 100,000 | 1.28×10^{-1} | 1.60×10^{-2} | 687.9 |
| Ours | 8000 | 100 | 5.94×10^{-2} | 4.92×10^{-3} | 39.4 |

5.5. High-dimensional scalability test. To evaluate the scalability of the proposed framework, we consider a fully coupled high-dimensional nonlinear Schrödinger model. The external potential is defined by an anisotropic quadratic form

$$(5.11) \quad V(\mathbf{r}) = \frac{1}{2} \mathbf{r}^\top \mathbf{A} \mathbf{r},$$

where $\mathbf{A} \in \mathbb{R}^{d \times d}$ is a randomly generated symmetric positive definite matrix. This construction induces strong coupling among all spatial dimensions and explicitly

precludes any separation-of-variables strategy. The interaction strength is set to $\beta = 2000$, and the computational domain is $\mathcal{D} = [-6, 6]^d$. In this regime, conventional grid-based discretization methods become infeasible due to the exponential growth of degrees of freedom with respect to the dimension d .

In the absence of high-dimensional reference solutions, we assess solution quality using the generalized virial theorem [14]. This theorem provides a stringent physical self-consistency criterion for ground states. Specifically, we define the virial residual ratio as

$$(5.12) \quad \mathcal{R}_{\text{vir}} = \frac{2\langle T \rangle + d\langle E_{\text{int}} \rangle}{2\langle V \rangle},$$

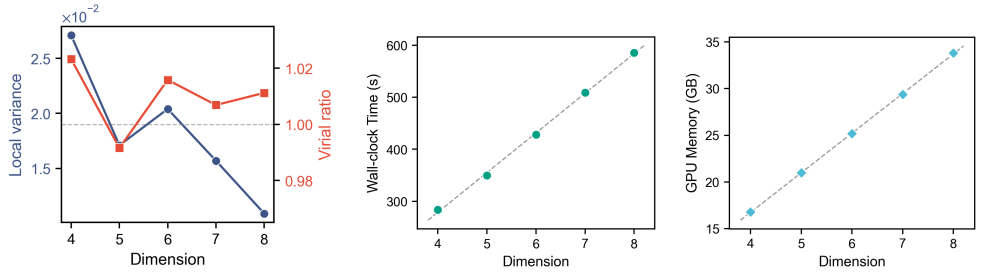
where $\langle T \rangle$, $\langle V \rangle$, and $\langle E_{\text{int}} \rangle$ denote the kinetic, potential, and interaction energy components, respectively. For an exact normalized ground state, this ratio equals unity; therefore, deviations from 1 provide a direct measure of physical inconsistency in the numerical approximation.

Numerical experiments were performed for dimensions $d = 4$ to 8 . HMC sampling was used with 15,000 walkers, and 12,000 samples were employed to estimate the normalization constant Z . All models were trained for 200 epochs. The results are summarized in Table 5, and the scaling trends are illustrated in Figure 6. As the dimension increases, the virial ratio remains consistently close to 1, with deviations confined to a few percent, while the local variance stays on the order of 10^{-2} . These observations confirm that the computed solutions satisfy the expected physical consistency conditions. Moreover, both the wall-clock time to convergence and the peak GPU memory usage exhibit approximately linear growth with dimension, with no evidence of exponential blow-up. Overall, these results demonstrate that the proposed neural VMC framework, combined with ADIS sampling and matrix-free Nyström-preconditioned Sobolev NGD, effectively captures strong inter-dimensional coupling and scales favorably to genuinely high-dimensional nonlinear Schrödinger problems.

Table 5: Physical consistency and computational cost for the high-dimensional fully coupled model, where $\kappa(\mathbf{A})$ denotes the condition number of the random matrix \mathbf{A} .

| Dim | $\kappa(\mathbf{A})$ | Time (s) | VRAM (GB) | Local variance | Virial ratio |
|-----|----------------------|----------|-----------|-----------------------|--------------|
| 4 | 2.09 | 284.0 | 16.8 | 2.71×10^{-2} | 1.02329 |
| 5 | 11.37 | 349.9 | 21.0 | 1.71×10^{-2} | 0.99159 |
| 6 | 9.56 | 428.1 | 25.2 | 2.04×10^{-2} | 1.01586 |
| 7 | 5.83 | 508.9 | 29.4 | 1.57×10^{-2} | 1.00690 |
| 8 | 12.61 | 585.7 | 33.8 | 1.09×10^{-2} | 1.01122 |

6. Conclusion and outlook. This paper presents a projected Sobolev NGD method for computing high-dimensional GPE ground states. By mapping the continuous gradient flow onto the neural tangent space via Galerkin projection, our framework ensures strict normalization and geometric consistency. To address the GPE's nonlinearity and dimensionality, we developed a hybrid ADIS-MCMC sampling strategy and a matrix-free Nyström PCG solver for efficient Gram matrix inversion. Numerical experiments demonstrate order-of-magnitude convergence improvements over PINN approaches, effectively mitigating the curse of dimensionality. Moreover, the learned



(a) Local variance and virial ratio versus dimension. (b) Wall-clock time to convergence versus dimension. (c) Peak GPU memory usage versus dimension.

Fig. 6: High-dimensional scalability analysis. (a) Local variance (blue, left axis) and virial ratio (red, right axis) as functions of dimension d , with the virial ratio remaining close to 1. (b) Wall-clock time to convergence exhibits approximately linear growth with respect to d (dashed line: linear fit). (c) Peak A100 GPU memory usage also scales linearly with dimension.

solutions serve as high-quality warm starts that significantly accelerate traditional solvers.

Several directions merit further investigation. First, extending the framework to rotating GPEs is critical. This task requires navigating complex energy landscapes and metastable vortices, potentially by integrating complex-valued neural networks. Second, computing excited states via penalty formulations or deflation strategies offers a natural extension. Finally, addressing the spectral bias of standard MLPs in high-frequency regimes, such as Anderson localization, calls for novel neural architectures tailored to multiscale structures.

REFERENCES

- [1] M. H. ANDERSON, J. R. ENSHER, M. R. MATTHEWS, C. E. WIEMAN, AND E. A. CORNELL, *Observation of Bose–Einstein condensation in a dilute atomic vapor*, Science, 269 (1995), pp. 198–201.
- [2] X. ANTOINE, A. LEVITT, AND Q. TANG, *Efficient spectral computation of the stationary states of rotating Bose–Einstein condensates by preconditioned nonlinear conjugate gradient methods*, J. Comput. Phys., 343 (2017), pp. 92–109.
- [3] V. ARMEGIOIU, J. CARRASQUILLA, S. MISHRA, J. MÜLLER, J. NYS, M. ZEINHOFER, AND H. ZHANG, *Functional neural wavefunction optimization*, arXiv preprint arXiv:2507.10835, (2025).
- [4] W. BAO, Z. CHANG, AND X. ZHAO, *Computing ground states of Bose–Einstein condensation by normalized deep neural network*, J. Comput. Phys., 520 (2025), p. 113486.
- [5] W. BAO AND Q. DU, *Computing the ground state solution of Bose–Einstein condensates by a normalized gradient flow*, SIAM J. Sci. Comput., 25 (2004), pp. 1674–1697.
- [6] J. BERMAN AND B. PEHERSTORFER, *Randomized sparse neural Galerkin schemes for solving evolution equations with deep networks*, Adv. Neural Inf. Process. Syst., 36 (2023), pp. 4097–4114.
- [7] A. BONFANTI, G. BRUNO, AND C. CIPRIANI, *The challenges of the nonlinear regime for physics-informed neural networks*, Adv. Neural Inf. Process. Syst., 37 (2024), pp. 41852–41881.
- [8] J. BRUNA, B. PEHERSTORFER, AND E. VANDEN-EIJNDEN, *Neural Galerkin schemes with active learning for high-dimensional evolution equations*, J. Comput. Phys., 496 (2024), p. 112588.
- [9] E. CANCÈS, G. KEMLIN, AND A. LEVITT, *Convergence analysis of direct minimization and self-consistent iterations*, SIAM J. Matrix Anal. Appl., 42 (2021), pp. 243–274.

- [10] G. CARLEO AND M. TROYER, *Solving the quantum many-body problem with artificial neural networks*, Science, 355 (2017), pp. 602–606.
- [11] H. CHEN, G. DONG, W. LIU, AND Z. XIE, *Second-order flows for computing the ground states of rotating Bose–Einstein condensates*, J. Comput. Phys., 475 (2023), p. 111872.
- [12] Z. CHEN, J. LU, Y. LU, AND X. ZHANG, *On the convergence of Sobolev gradient flow for the Gross–Pitaevskii eigenvalue problem*, SIAM J. Numer. Anal., 62 (2024), pp. 667–691.
- [13] Z. CHEN, J. MCCARRAN, E. VIZCAINO, M. SOLJAČIĆ, AND D. LUO, *TENG: Time-evolving natural gradient for solving PDEs with deep neural nets toward machine precision*, arXiv preprint arXiv:2404.10771, (2024).
- [14] F. DALFOVO, S. GIORGINI, L. P. PITAEVSKII, AND S. STRINGARI, *Theory of Bose–Einstein condensation in trapped gases*, Rev. Mod. Phys., 71 (1999), pp. 463–512.
- [15] I. DANAILA AND P. KAZEMI, *A new Sobolev gradient method for direct minimization of the Gross–Pitaevskii energy with rotation*, SIAM J. Sci. Comput., 32 (2010), pp. 2447–2467.
- [16] I. DANAILA AND B. PROTAS, *Computation of ground states of the Gross–Pitaevskii functional via Riemannian optimization*, SIAM J. Sci. Comput., 39 (2017), pp. B1102–B1129.
- [17] F. DANGEL, J. MÜLLER, AND M. ZEINHOFER, *Kronecker-factored approximate curvature for physics-informed neural networks*, Adv. Neural Inf. Process. Syst., 37 (2024), pp. 34582–34636.
- [18] Z. DENIS AND G. CARLEO, *Accurate neural quantum states for interacting lattice bosons*, Quantum, 9 (2025), p. 1772.
- [19] C. M. DION AND E. CANCÈS, *Ground state of the time-independent Gross–Pitaevskii equation*, Comput. Phys. Commun., 177 (2007), pp. 787–798.
- [20] P. A. DIRAC, *Note on exchange phenomena in the Thomas atom*, in Math. Proc. Cambridge Philos. Soc., vol. 26, 1930, pp. 376–385.
- [21] Y. DU AND T. A. ZAKI, *Evolutional deep neural network*, arXiv preprint arXiv:2103.09959, (2021).
- [22] Z. FENG AND Q. TANG, *On preconditioned Riemannian gradient methods for minimizing the Gross–Pitaevskii energy functional: algorithms, global convergence and optimal local convergence rate*, arXiv preprint arXiv:2510.13516, (2025).
- [23] Z. FRANGELLA, J. A. TROPP, AND M. UDELL, *Randomized Nyström preconditioning*, SIAM J. Matrix Anal. Appl., 44 (2023), pp. 718–752.
- [24] J. FRENKEL, *Wave Mechanics: Advanced General Theory*, Clarendon Press, 1934.
- [25] J. J. GARCÍA-RIPOLL AND V. M. PÉREZ-GARCÍA, *Optimizing Schrödinger functionals using Sobolev gradients: applications to quantum mechanics and nonlinear optics*, SIAM J. Sci. Comput., 23 (2001), pp. 1316–1334.
- [26] A. GUZMÁN-CORDERO, F. DANGEL, G. GOLDSHLAGER, AND M. ZEINHOFER, *Improving energy natural gradient descent through Woodbury, momentum, and randomization*, arXiv preprint arXiv:2505.12149, (2025).
- [27] P. HENNING, L. HUYNH, AND D. PETERSEIM, *Metric-driven numerical methods*, arXiv preprint arXiv:2512.10083, (2025).
- [28] P. HENNING AND E. JARLEBRING, *The Gross–Pitaevskii equation and eigenvector nonlinearities: numerical methods and algorithms*, SIAM Rev., 67 (2025), pp. 256–317.
- [29] P. HENNING AND D. PETERSEIM, *Sobolev gradient flow for the Gross–Pitaevskii eigenvalue problem: Global convergence and computational efficiency*, SIAM J. Numer. Anal., 58 (2020), pp. 1744–1772.
- [30] M. F. HERBST, A. LEVITT, AND E. CANCÈS, *DFTK: A Julian approach for simulating electrons in solids*, Proc. JuliaCon Conf., 3 (2021), p. 69.
- [31] J. HERMANN, Z. SCHÄTZLE, AND F. NOÉ, *Deep-neural-network solution of the electronic Schrödinger equation*, Nat. Chem., 12 (2020), pp. 891–897.
- [32] E. JARLEBRING, S. KVAAL, AND W. MICHELS, *An inverse iteration method for eigenvalue problems with eigenvector nonlinearities*, SIAM J. Sci. Comput., 36 (2014), pp. A1978–A2001.
- [33] K. JIANG, X. LI, Y. MA, J. ZHANG, P. ZHANG, AND Q. ZHOU, *Irrational-window-filter projection method and application to quasiperiodic Schrödinger eigenproblems*, SIAM J. Numer. Anal., 63 (2025), pp. 564–587.
- [34] T. KAO, H. ZHANG, L. ZHANG, AND J. ZHAO, *pETNs: Partial evolutionary tensor neural networks for solving time-dependent partial differential equations*, CSIAM Trans. Appl. Math., 6 (2025), pp. 862–891.
- [35] H. KIM AND T. A. ZAKI, *Multi evolutional deep neural networks (Multi-EDNN)*, J. Comput. Phys., 531 (2025), p. 113910.
- [36] D. P. KINGMA AND J. BA, *Adam: A method for stochastic optimization*, in International Conference on Learning Representations (ICLR), 2015.

- [37] Z. KONG, J. Z. YANG, C. YUAN, AND X. ZHAO, *Toward fast, accurate and robust AI prediction of ground states in rotating BEC*, arXiv preprint arXiv:2511.07489, (2025).
- [38] Q. LI, Y. LIU, J. ZHAO, AND W. ZHU, *MAD-NG: Meta-auto-decoder neural Galerkin method for solving parametric partial differential equations*, arXiv preprint arXiv:2512.21633, (2025).
- [39] E. H. LIEB, R. SEIRINGER, AND J. YNGVASON, *Bosons in a trap: A rigorous derivation of the Gross-Pitaevskii energy functional*, Phys. Rev. A, 61 (2000), p. 043602.
- [40] D. W. MARQUARDT, *An algorithm for least-squares estimation of nonlinear parameters*, J. Soc. Indust. Appl. Math., 11 (1963), pp. 431–441.
- [41] J. MARTENS, *New insights and perspectives on the natural gradient method*, J. Mach. Learn. Res., 21 (2020), pp. 1–76.
- [42] N. METROPOLIS, A. W. ROSENBLUTH, M. N. ROSENBLUTH, A. H. TELLER, AND E. TELLER, *Equation of state calculations by fast computing machines*, J. Chem. Phys., 21 (1953), pp. 1087–1092.
- [43] R. M. NEAL, *MCMC using Hamiltonian dynamics*, in *Handbook of Markov Chain Monte Carlo*, S. Brooks, A. Gelman, G. Jones, and X.-L. Meng, eds., Chapman & Hall/CRC, 2011, pp. 113–162.
- [44] L. NURBEKYAN, W. LEI, AND Y. YANG, *Efficient natural gradient descent methods for large-scale PDE-based optimization problems*, SIAM J. Sci. Comput., 45 (2023), pp. A1621–A1655.
- [45] T. OZAWA, H. M. PRICE, A. AMO, N. GOLDMAN, M. HAFEZI, L. LU, M. C. RECHTSMAN, D. SCHUSTER, J. SIMON, O. ZILBERBERG, ET AL., *Topological photonics*, Rev. Mod. Phys., 91 (2019), p. 015006.
- [46] D. PETERSEIM, J.-F. PIETSCHMANN, J. PÜSCHEL, AND K. RUESS, *Neural network acceleration of iterative methods for nonlinear Schrödinger eigenvalue problems*, arXiv preprint arXiv:2507.16349, (2025).
- [47] D. PETERSEIM, J. PÜSCHEL, AND T. STYKEL, *Energy-adaptive Riemannian conjugate gradient method for density functional theory*, arXiv preprint arXiv:2503.16225, (2025).
- [48] D. PFAU, J. S. SPENCER, A. G. MATTHEWS, AND W. M. C. FOULKES, *Ab initio solution of the many-electron Schrödinger equation with deep neural networks*, Phys. Rev. Res., 2 (2020), p. 033429.
- [49] M. RAISI, P. PERDIKARIS, AND G. E. KARNIADAKIS, *Physics-informed neural networks: A deep learning framework for solving forward and inverse problems involving nonlinear partial differential equations*, J. Comput. Phys., 378 (2019), pp. 686–707.
- [50] N. SCHWENCKE, C. ROUSSELOT, A. SHILOVA, AND C. FURTLEHNER, *AMStraMGRAM: Adaptive multi-cutoff strategy modification for anagram*, arXiv preprint arXiv:2510.15998, (2025).
- [51] S. SORELLA, *Green function Monte Carlo with stochastic reconfiguration*, Phys. Rev. Lett., 80 (1998), pp. 4558–4561.
- [52] M. TANCIK, P. SRINIVASAN, B. MILDENHALL, S. FRIDOVICH-KEIL, N. RAGHAVAN, U. SINGHAL, R. RAMAMOORTHI, J. BARRON, AND R. NG, *Fourier features let networks learn high frequency functions in low dimensional domains*, Adv. Neural Inf. Process. Syst., 33 (2020), pp. 7537–7547.
- [53] M. UEDA, *Spinor Bose–Einstein condensates*, Contemp. Phys., 63 (2022), pp. 106–115.
- [54] L. L. VITERITTI, R. RENDE, AND F. BECCA, *Transformer variational wave functions for frustrated quantum spin systems*, Phys. Rev. Lett., 130 (2023), p. 236401.
- [55] D. WU, R. ROSSI, F. VICENTINI, N. ASTRAKHANTSEV, F. BECCA, X. CAO, J. CARRASQUILLA, F. FERRARI, A. GEORGES, M. HIBAT-ALLAH, ET AL., *Variational benchmarks for quantum many-body problems*, Science, 386 (2024), pp. 296–301.
- [56] M. ZEINHOFER, R. MASRI, AND K.-A. MARDAL, *A unified framework for the error analysis of physics-informed neural networks*, IMA J. Numer. Anal., (2024), p. drae081.
- [57] J. ZHANG, S. ZHANG, AND G. LIN, *Low-rank adaptation of evolutionary deep neural networks for efficient learning of time-dependent PDEs*, arXiv preprint arXiv:2509.16395, (2025).